Atmos. Chem. Phys. Discuss., 14, 19315–19356, 2014
www.atmos-chem-phys-discuss.net/14/19315/2014/
doi:10.5194/acpd-14-19315-2014

Atmospheric Chemistry and Physics Discussions

Gauss-Seidel Limb Scattering (GSLS) radiative transfer model development in support of the Ozone Mapping and Profiler Suite (OMPS) Limb Profiler mission

R. Loughman[1], D. Flittner[2], E. Nyaku[1], and P. K. Bhartia[3]

[1]Department of Atmospheric and Planetary Sciences, Hampton University, Hampton, Virginia, USA
[2]Climate Science Branch, NASA Langley Research Center, Hampton, Virginia, USA
[3]Atmospheric Chemistry and Dynamics Laboratory, NASA Goddard Space Flight Center, Greenbelt, Maryland, USA

Received: 24 June 2014 – Accepted: 1 July 2014 – Published: 28 July 2014

Correspondence to: R. Loughman (robert.loughman@hamptonu.edu)

Published by Copernicus Publications on behalf of the European Geosciences Union.

Abstract

The Gauss-Seidel Limb Scattering (GSLS) radiative transfer (RT) model simulates the transfer of solar radiation through the atmosphere, and is imbedded in the retrieval algorithm used to process data from the Ozone Mapping and Profiler Suite (OMPS) Limb Profiler (LP), which was launched on the Suomi NPP satellite in October 2011. A previous version of this model has been compared with several other limb scattering RT models in previous studies, including Siro, MCC++, CDIPI, LIMBTRAN, SASKTRAN, VECTOR, and McSCIA. To address deficiencies in the GSLS radiance calculations revealed in earlier comparisons, several recent changes have been added that improve the accuracy and flexibility of the GSLS model, including:

1. Improved treatment of the variation of the extinction coefficient with altitude, both within atmospheric layers and above the nominal top of the atmosphere (TOA).
2. Addition of multiple scattering source function calculations at multiple zeniths along the line of sight (LOS).
3. Re-introduction of the ability to simulate vector (polarized) radiances.
4. Introduction of variable surface properties along the limb LOS, with minimal effort required to add variable atmospheric properties along the LOS as well.
5. Addition of the ability to model multiple aerosol types within the model atmosphere.

The model improvements numbered 1–3 above are verified by comparison to previously published results (using standard radiance tables whenever possible), demonstrating significant improvement in cases for which previous versions of the GSLS model performed poorly. The single-scattered radiance errors that were as high as 4 % in earlier studies are now generally reduced to < 0.5 %, while total radiance errors generally decline from > 10 % to 1–2 %. In all cases, the height dependence of the GSLS radiance error is greatly reduced.

ACPD
14, 19315–19356, 2014

1 Introduction

Incoming solar irradiance interacts with the Earth's atmosphere as it penetrates downwards towards the surface. The nature of these interactions depends upon the composition of the atmospheric layers, and this fact has been exploited by many successful remote sensing techniques that use observations of the radiation that exits the atmosphere to learn about atmospheric composition. Several viewing geometries have been exploited in this way, such as observing downwelling radiation at the Earth's surface, upwelling radiation at the top of the atmosphere (TOA), as well as the internal radiation field within the atmosphere. Upwelling radiance at the TOA along a line of sight (LOS) that passes near (but above) the horizon, and therefore does not intersect the Earth's surface, is commonly known as limb scattering (LS), as illustrated in Fig. 1. LS observations have been successfully employed to infer the properties of the Earth's atmosphere in several past and present remote sensing missions, such as SOLSE/LORE (McPeters et al., 2000), OSIRIS (Llewellyn et al., 2004), SCIAMACHY (Bovensmann et al., 1999), SAGE III (Rault, 2005), GOMOS (Kyrölä et al., 2004), and OMPS LP (Flynn et al., 2006).

An essential tool for interpretation of LS observations is a radiative transfer (RT) model capable of simulating the LS radiance field for a specified atmosphere. Many models have been developed to simulate LS radiances, including the DART (Whitney, 1977), Siro (Oikarinen et al., 1999), LIMBTRAN (Griffioen and Oikarinen, 2000), CDIPI (Rozanov et al., 2001), VECTOR (McLinden et al., 2002), MCC++ (Postylyakov, 2004), GSLS (Loughman et al., 2004), McSCIA (Spada et al., 2006), and SASKTRAN (Bourassa et al., 2008) models. A previous paper (Loughman et al., 2004, called L04 herein) assesses the consistency of several LS RT models at an earlier stage in their development, and has provided a useful benchmark for subsequent RT model development (Spada et al., 2006; Bourassa et al., 2008; McLinden and Bourassa, 2010). The L04 paper highlighted several shortcomings in the GSLS model, and improving

ACPD
14, 19315–19356, 2014

the model by rectifying those shortcomings is the primary motivation for the present work.

The GSLS model is built from several previous models (Herman et al., 1994, 1995) and is summarized in (Loughman et al., 2004), abbreviated as L04 herein. It has been used for retrieval applications on missions including SOLSE/LORE (Flittner et al., 2000), SAGE III (Rault, 2005; Rault and Taha, 2007), GOMOS (Taha et al., 2008), and OMPS LP (Rault and Loughman, 2013). These retrieval algorithms have shown a remarkable degree of accuracy despite the shortcomings of the GSLS model, but development of a more accurate version of the GSLS model is desirable for the purpose of interpreting residuals (differences between measured radiances and radiances calculated for the desired model atmosphere). This paper is devoted to describing and demonstrating the improvements made to the GSLS model.

2 Optical path length improvement

The L04 radiance comparison study notes a bias in the GSLS single-scattered (SS) radiances relative to the SS radiances computed by the Siro model, which served as the radiance benchmark in the L04 study. This bias arises from the approximation used to calculate the limb optical path length τ through a layer in the L04 version of GSLS. The correct calculation of τ requires integrating the extinction coefficient β along the LOS through the relevant layer.

$$\tau = \int_0^s \beta \mathrm{d}s' \tag{1}$$

In both L04 and the current study, the influence of refraction is neglected, so it is appropriate to refer to the path taken by a photon as a straight line, with the geometric path length coordinate s' increasing from 0 to s as the photon traverses the layer. The model atmosphere is defined by specifying the value of β at discrete altitudes within

ACPD
14, 19315–19356, 2014

the model atmosphere (by specifying values from which β can be derived, such as the number densities and cross-sections for various sources of extinction). In both L04 and this study, the model atmosphere consists of 100 layers, each 1 km thick, with the top of the atmosphere 100 km above the Earth's surface. (The significance of the "top of the atmosphere" in the RT model is discussed further in Sect. 5.)

This atmospheric definition provided each model in the L04 comparison with consistent values of β at the top (β_t) and bottom (β_b) of each layer, but allowed the various RT models to make different assumptions about how β should vary within the atmospheric layers. In the L04 version of GSLS, the average value of β within the layer is multiplied by the layer geometric path length s to determine τ in all layers except the tangent layer; that is,

$$\tau = \frac{s(\beta_t + \beta_b)}{2} \quad (2)$$

As noted in L04, the Siro model makes a more accurate approximation, by assuming that β varies as a linear function of altitude within each layer. Figure 4 of L04 shows that this assumption has a significant impact on the LS radiance calculation, particularly for the single-scattered (SS) radiance: the SS radiances calculated by the L04 GSLS model agree well with the SS radiances produced by other models that use the approximation given in Eq. (2), and also agree with Siro SS radiances for tangent height $h \approx 10$ km. But the SS radiances calculated by models that use Eq. (2) diverge from the Siro SS radiances as h increases, disagreeing by as much as 1 % for $h = 60$ km. When the Siro model was modified to calculate τ as shown in Eq. (2), the SS radiance differences were greatly reduced.

Figures 2–3 collect information shown in Figs. 6–8 of L04 in a different format, showing the difference between the L04 GSLS SS radiances and the Siro SS radiances for the cases listed in Table 1. Cases are specified by the wavelength λ, the solar zenith angle at the tangent point (TP) for the LOS θ_T, and the relative azimuth angle at the TP ϕ_T. The differences in Figs. 2–3 range from −2.6 % to +3.6 %. In Figs. 4–5, Siro SS radiances are instead compared to the current GSLS SS radiances. Implementation

ACPD
14, 19315–19356, 2014

of the linear variation of β with altitude in the current GSLS model both reduces the disagreement range (now −0.4 % to +0.8 %) and virtually eliminates the altitude dependence of the disagreement. The only outliers in this comparison are the ($\theta_T = 60^\circ$, $\phi_T = 20^\circ$, $\lambda = 600$ nm) case (which disagrees with Siro by up to −1.5 % in Fig. 4) and the ($\theta_T = 80^\circ$, $\phi_T = 20^\circ$, $\lambda = 600$ nm) case (which disagrees with Siro by up to +1.5 % in Fig. 5). The comparison in Fig. 8a of L04 shows similar disagreement between GSLS and the other models (MCC++, CDIPI and LIMBTRAN) for these cases, suggesting that a problem existed in the L04 GSLS SS radiances for those two cases, and that the problem remains unsolved in the current GSLS model.

The generally close agreement between Siro and current GSLS SS radiances is not surprising, since both models now use the same approximation for the variation of β within atmospheric layers. The method used to compute τ when β varies linearly with altitude in the current GSLS model is presented more fully in Appendix A. It is relatively straightforward, admitting an analytic solution and requiring only application of integral forms that are readily available in standard references. Its computation cost is therefore modest (producing a negligible increase in calculation time).

As shown in Figs. 2–5, implementing the linear variation of β with altitude produced significant improvement in the SS radiance comparison. Similar modifications were also made to allow the GSLS model to compute layer path lengths the same way in the multiple scattering (MS) source function calculations as well. As noted in L04, the MS source functions are computed using a modified version of the "cone code" described in (Herman et al., 1994, 1995). Given the short path lengths between the zenith and conical boundary and the relatively small contribution of LS paths to the overall value of the MS source function, this modification produced a negligible change in the MS radiance calculation.

ACPD
14, 19315–19356, 2014

3 Multiple MS zeniths improvement

As described in Appendix A of L04, the L04 GSLS model computes the MS source function for the single zenith that intersects the TP for the LOS of interest (see $\vec{OT}$ in Fig. 6). This approximation contributes to the speed of the L04 GSLS model, at the cost of lost accuracy for some MS radiance calculations in which the MS source function varies significantly along the LOS. The total scattered radiances (TS = SS + MS) calculated by the L04 GSLS model differ from the Siro reference radiances by as much as 12 % for surface reflectivity $R = 0.95$ and $\theta_T \leq 80^\circ$, as shown in Fig. 7 (which displays information taken from the Figs. 6–8 of L04 in modified form). For cases when the LOS is optically thin (such as Fig. 8), the radiance is dominated by contributions from the layers near the TP, so use of the MS source function values calculated at the TP for the entire LOS integration causes little error. But the L04 GSLS radiances differ most from the Siro radiances for ultraviolet (UV) wavelengths (325 and 345 nm) at small tangent heights ($h < 30$ km), where the LOS optical path becomes large and contributions from the layers between the TP and the observer become more significant, as illustrated in Figs. 9–10. Note that the current GSLS model uses approximations that prevent it from calculating MS source functions properly when the sun is at or below the horizon, so cases that require such calculations will not be analyzed in this study.

The current GSLS model has been modified to allow computation of MS source functions at several zeniths along the LOS (e.g., $\vec{OA}$, $\vec{OP}$, $\vec{OT}$, $\vec{OQ}$, $\vec{OE}$ in Fig. 6). This modification allows better representation of the MS source function, as shown by the improved total scatter (TS) radiance agreement with Siro in Fig. 11. The cases shown in Fig. 7 for L04 GSLS radiances are repeated in Fig. 11 for current GSLS radiances, for which TS radiance differences relative to Siro are reduced to ≤ 4 %. The other LS RT models mentioned earlier either already contain a multi-zenith capability for MS source function calculations (e.g., CDIPI, VECTOR, LIMBTRAN, and SASKTRAN) or explicitly simulate each photon, eliminating the need for this capability (e.g., Siro, MCC++, and McSCIA).

ACPD
14, 19315–19356, 2014

A limited study was done to assess the required number and placement of the MS zeniths along the LOS to reach a given standard of accuracy. In this study, the scene reflectivity R was set to 0.95 (to maximize the impact of MS on the TS radiance). The viewing geometry was varied as described in Table 2. As a reference, the current GSLS RT model was run with 143 MS zeniths selected. First, a MS zenith was placed to intersect each point for which the LOS at $h = 30$ km intersects an atmospheric level. This yields 141 MS zenith values, with the remaining 2 MS zenith values set at the zeniths for which the LOS with $h = 0$ km intersects the TOA at each end of the LOS. These reference calculations were then compared to the results obtained with just 1 MS zenith (at the TP of the LOS). For the purpose of this study, additional MS zeniths were gradually added until the difference from the reference calculation (with 143 MS zeniths) became $< 0.2\%$ at all values of h and λ.

Placement of the additional MS zeniths was motivated by Figs. 8–10, which demonstrate how the layers that contribute most to the radiance shift from the TP towards the observer as h decreases, particularly for the optically thicker UV wavelengths considered (325, 345 nm). Figure 12 is color-coded to indicate the number of MS zeniths required to meet the 0.2% difference standard. The sequence and placement of the MS zeniths was:

1. Zenith that intersects the LOS at the TP (i.e. $\vec{OA}$ in Fig. 6).
2. Zenith that intersects the LOS at the TOA on the "near side" (MS zenith is between TP and observer, i.e. $\vec{OA}$ in Fig. 6)
3. Zenith that intersects the LOS at the TOA on the "far side" (TP is between MS zenith and observer, i.e. $\vec{OE}$ in Fig. 6)
4. Zenith that intersects the LOS at the level immediately above the TP on the "near side" (i.e. $\vec{OP}$ in Fig. 6)

ACPD
14, 19315–19356, 2014

5. Zenith that intersects the LOS at the level immediately above the TP on the "far side" (i.e. $\vec{OQ}$ in Fig. 6)

6. Zenith added to the "near side" of the LOS, placed by experimentation with the cases listed in Table 2). Best results were obtained when the angle between the TP MS zenith ($\vec{OT}$ in Fig. 6) and the new MS zenith = 2.86159°.

The SS radiance is unaffected by the number of MS zeniths used, and the change in TS radiance due to adding MS zeniths is slight when $\theta_T \approx 0°$ (sun nearly overhead at the TP) or $\phi_T \approx 90°$ (LOS nearly perpendicular to the solar plane), because those conditions minimize the variation of the solar illumination along the LOS. As the sun approaches the horizon or the LOS becomes more aligned with the solar plane, the importance of adding MS zeniths grows. Comparing Fig. 7 to Fig. 11 shows that the radiances at small tangent heights (h = 10 km is the smallest included in this analysis) are most affected by the placement of MS zeniths. The ultraviolet wavelengths (for which the atmosphere is optically thicker) are also most sensitive to the details of MS zenith placement.

As shown in Fig. 12, the L04 GSLS model meets the standard of TS radiance accuracy better than 0.2% only for cases with $\phi_T = 90°$. But 2 MS zeniths are sufficient for some viewing geometries with small θ_T and/or ϕ_T near 90°, and 3 MS zeniths suffice for a large range of viewing conditions. Adding the 4th and 5th MS zeniths produce marginal improvement, but 6 MS zeniths suffice for nearly every remaining case. The cases that require > 6 MS zeniths to meet the criterion of TS radiance accuracy better than 0.2% arise at ultraviolet wavelengths with $\theta_T = 85°$ and ϕ_T far from 90°. In such cases, part of the LOS is often below the horizon, and therefore the current GSLS model performance cannot be trusted in any case. The question of how many MS zeniths are necessary under such "twilight" conditions is not addressed by the present study.

Adding additional MS zeniths clearly increases the computational effort of the calculation, so the trade-off between accuracy and run-time must be carefully considered for

ACPD
14, 19315–19356, 2014

a given application. For example, a GSLS run that uses 6 MS zeniths (the maximum required for the cases studied) takes roughly twice as long as a GSLS run with 2 MS zeniths (the minimum required for any case with $\phi_T \neq 90^\circ$). Also note that the GSLS modifications described in this section make it easy to vary the surface reflection properties along the LOS. With minor code modifications, variation of the atmosphere along the LOS could also be added.

Finally, it must be noted that the current GSLS TS radiances uniformly exceed the Siro TS values by a small amount (1–2 %) for the cases shown in Fig. 11. Some brief experiments (not included in this paper) indicate that the observed over-estimate increases with increasing R and with decreasing θ_T, clearly suggesting that the treatment of radiance reflected by the surface that underlies the model atmosphere is a possible source of error. The reason for this discrepancy is unknown, but it may be related to the fact that RT models using flat (or pseudo-spherical, like the current GSLS) atmospheres for MS calculations tend to over-estimate upwelling radiation, as noted by (McLinden and Bourassa, 2010).

4 Polarization improvement

The L04 GSLS model calculated polarized (vector) radiances properly, but this capability was not maintained as the L04 GSLS model was adapted to calculate unpolarized (scalar) radiances for the OMPS LP retrieval algorithms (Rault and Loughman, 2013). Although the scalar RT equation is an approximation with no clear theoretical basis (Mishchenko et al., 1994), this defect in the calculated radiances was not significant for the purpose of the OMPS LP retrievals, because the radiance error largely cancels out given the tangent height normalization and wavelength grouping used in those retrieval algorithms (Loughman et al., 2005). However, the interpretation of radiance residuals is complicated by the neglect of polarization, so the current GSLS model has been modified to restore its vector radiance capability.

ACPD
14, 19315–19356, 2014

The accuracy of the vector radiances calculated by the current GSLS model were verified in two ways. First, we confirmed that the current GSLS model duplicates the L04 GSLS polarized radiances shown in Fig. 3 of (Loughman et al., 2004) to the 0.01 % level, provided that the optical path lengths were calculated as shown in Eq. (2). The second set of comparisons involved the results tabulated by Natraj et al. (2009), which represent an updated version of the well-known Rayleigh scattering calculations initially produced by Coulson et al. (1960). The Natraj et al. (2009) comparisons cover the cases listed in Table 3. To enable this comparison, the current GSLS model was run as a "flat atmosphere" model (by increasing the Earth's radius by a factor of 1000). The emerging radiances at the TOA and the surface match the Natraj et al. (2009) results to better than 1.4 % for all LOS, with agreement better than 0.5 % except in a few cases.

The scalar LS radiances differ significantly from correct polarized radiances by as much as −4 % to +7 %, as shown in Fig. 13. The overall behavior of these curves follows the expected pattern (Mishchenko et al., 1994), with the largest errors appearing at 345 nm, when Rayleigh scattering dominates, just a few scattering events are likely for a typical photon (atmospheric optical depth is ≈ 1), atmospheric absorption is weak, and surface reflectivity R is small. The error is greatest when the SS angle at the TP $\Theta_T \approx 90^\circ$, which occurs near the mid-point of the NPP OMPS LP orbit (in the tropics). As noted in L04, the SS angle Θ_T is related to the solar zenith angle and relative azimuth angle at the TP (θ_T and ϕ_T, respectively) by

$$\cos\Theta_T = \sin\theta_T \cos\phi_T \tag{3}$$

5 Chapman layer improvement

The "top of the atmosphere" for the L04 GSLS model atmosphere was mentioned in Sect. 2. Of course, a real atmosphere does not abruptly end at any particular height, but instead becomes more and more rarefied as height increases (consistent with hydrostatic balance, in the long-term average). The RT model atmosphere is typically

ACPD
14, 19315–19356, 2014

specified (by profiles of pressure, temperature, aerosols, absorbing gases, etc.) to some notional "top of the atmosphere" (TOA) altitude. The altitude at which the TOA can be placed depends on the application for which the RT calculations are done, which determines the required accuracy of the radiances. The atmosphere above the TOA can be treated in several ways, which also influences the necessary TOA for a particular application. The simplest approach is to ignore the region above the TOA entirely (effectively treating it as a vacuum), but this produces discontinuous atmospheric profiles that can significantly deform the radiance profiles.

A better approach was developed by Chapman (1931), who modeled the profile of each constituent in an atmosphere above a certain level as falling off exponentially with height, at a rate governed by the scale height of the constituent. This approach remains relatively simple, but it avoids discontinuity of the model atmosphere, and also has some degree of physical realism (for example, the molecular number density in an isothermal atmosphere will decay with a constant scale height, to the extent that variations of gravity with altitude can be ignored). An atmospheric region that behaves in this way is commonly known as a "Chapman layer".

The L04 GSLS model contained an option to treat the atmospheric region from the TOA to infinity as a Chapman layer, following the computational strategy suggested by Fitzmaurice (1964). However, this option was erroneously disabled by a switch in the L04 GSLS model, causing the atmosphere above the TOA to be treated like a vacuum. (This switch was put in place to enable comparisons with RT models that lacked a Chapman layer capability, but was accidentally never disengaged at the conclusion of those studies).

In the current GSLS model, the Chapman layer routine is restored to proper functionality. Although such details have little effect, the example shown in Fig. 14 corresponds to $\theta_T = 60^\circ$, $\phi_T = 90^\circ$, $R = 0$, and $\lambda = 345$ nm for the atmosphere used in the L04 study. Figure 14 shows that when the TOA is sufficiently high above the maximum tangent height h of interest, the inclusion or exclusion of the Chapman layer has little influence on the LS radiance. For example, the TOA was set at 100 km in the L04 comparisons,

ACPD
14, 19315–19356, 2014

while the radiance comparisons ended at $h = 60$ km, so the lack of a Chapman layer had a negligible impact in that study. The absolute value of the percentage error in radiance due to exclusion of the Chapman layer under those conditions is $< 0.02\%$ for $h < 60$ km, $< 0.07\%$ for $h < 70$ km, and $< 0.5\%$ for $h < 80$ km. Including the Chapman layer rapidly becomes more consequential as the TOA and the maximum h of interest move closer together: for example, the radiance error at $h = 70$ km approaches 8% when the TOA = 80 km and the Chapman layer is excluded, but is reduced to $< 3\%$ when the TOA = 80 km and the Chapman layer is included.

6 Variable aerosol size distribution improvement

Stratospheric aerosol measurement campaigns (Deshler et al., 2003) clearly demonstrate that the aerosol size distribution (ASD) varies significantly with altitude (typically with smaller particles at higher altitudes). The L04 GSLS model was incapable of including such variation – the same aerosol ASD and optical properties (refractive indices) were used for all aerosols in the atmosphere, regardless of altitude. The current GSLS model has been updated to allow the aerosol ASD and optical properties (and therefore the aerosol phase function) to vary with altitude.

Figure 15 shows two bi-modal log-normal ASDs that were created by averaging the individual ASD properties (aerosol concentration N, aerosol mode radius r and aerosol mode standard deviation σ) retrieved during 6 balloon flights over Laramie, Wyoming during 2012 (Deshler, 2013). The red line indicates the resulting ASD for altitude $z =$ 20 km (ASD20), while the green line indicates the ASD at $z = 25$ km (ASD25). The details of these two size distributions are given in Table 4.

As a crude indication of the significance of the ASD for LS radiances, Fig. 16 compares the TS radiances calculated when the entire atmosphere uses ASD20 to the TS radiances calculated when the entire atmosphere uses ASD25. The aerosol phase function differs between the two cases, but other quantities (such as the aerosol extinction coefficient) are fixed in each case. The magnitude of the radiance sensitivity to

ACPD
14, 19315–19356, 2014

ASD at 600 nm can be as large as 20 %, suggesting that an over-simplified portrayal of the stratospheric ASD (e.g., excluding the phase function variation with altitude) may be a significant source of aerosol extinction retrieval error.

7 Conclusions

The GSLS RT model has been updated relative to the L04 version, significantly improving the calculated limb scattered radiances. The single scattered radiance error now is generally < 0.5 % and the total radiance error has been reduced to the 1–2 % level. These accuracy gains arise primarily from improving the treatment of extinction variation within atmospheric layers (described in Sect. 2) and adding calculations of the multiple scattering source function at multiple zeniths along the limb scattering line of sight (described in Sect. 3). The required number of zeniths for accurate radiance calculations is shown to be relatively modest: three or less is sufficient for most lines of sight, and six is sufficient for all cases except twilight conditions. The ability to model surface reflectivity variations and multiple aerosol types within the model atmosphere have also been added to the GSLS model, enabling more realistic model atmospheres to be simulated. As shown in previous studies, the OMPS LP retrieval algorithms are resilient, tolerating numerous radiative transfer model approximations without significantly changing the retrieved profiles, but these model improvements will make the GSLS model more useful for understanding OMPS LP radiance residuals. Proposed future work includes fully implementing the ability to vary the atmospheric profiles along the limb line of sight.

Appendix A

As noted in Eq. (1), the optical path length through a layer τ is given by the integral of the extinction coefficient β along the LOS through the layer. If we assume that β varies linearly with height between the endpoints of the path (emulating the method

ACPD
14, 19315–19356, 2014

used by the Siro model, as described in L04), then the integral shown in Eq. (1) has an analytic solution that can be obtained from standard tables of integrals (for both tangent and non-tangent paths). We will use the subscripts 0 and 1 to indicate the values of various quantities at the endpoints of the LOS, corresponding to the lower and upper limits of the integral in Eq. (1), respectively. For a spherical Earth, r_0 and r_1 indicate the distances from the center of the Earth to endpoints 0 and 1, respectively (for example, $r_0 = OQ$ and $r_1 = OT$ in Fig. 6). Similarly, β_0 and β_1 represent the values of the extinction coefficient at endpoints 0 and 1. Finally, the angle between the LOS (in the direction the radiation is traveling) and the zenith line that intersects the LOS at r_0 (outwards from the center of the Earth) is denoted by θ (i.e., the angle θ_Q in Fig. 6).

If we assume that β is a linear function of altitude (or r) within the relevant layer, then the following expressions obviously follow:

$$\beta(r) = Ar + B \tag{A1}$$

where

$$A = (\beta_0 - \beta_1)/(r_0 - r_1)$$
$$B = \beta_0 - A\, r_0 \tag{A2}$$

Substituting Eq. (A1) into Eq. (1) yields

$$\tau = \int_0^s (A\, r' + B)\mathrm{d}s' = Bs + A\int_0^s r'\mathrm{d}s' \tag{A3}$$

To evaluate Eq. (A3), the variation of r' along the LOS from r_0 to r_1 must be characterized. This can be determined from the Law of Cosines as

$$r' = \sqrt{s'^2 - 2s' r_0 \cos(\pi - \theta) + {r_0}^2} = \sqrt{s'^2 + 2s' r_0 \cos\theta + {r_0}^2}$$
$$r' = \sqrt{cs'^2 + bs' + a} \tag{A4}$$

ACPD
14, 19315–19356, 2014

As implied in Eq. (A4), $a = r_0^2$, $b = 2r_0\cos\theta$, and $c = 1$. Substituting Eq. (A4) into Eq. (A3) yields an integral that can be evaluated analytically based on CRC (1984), Eqs. (242) and (237), using the shorthand $k^{-1} = (4ac - b^2)/4c = r_0^2\sin^2\theta$:

$$\int_0^s \mathrm{d}s' \sqrt{cs'^2 + bs' + a}$$

$$= \left\{ \frac{2cs' + b}{4c} \sqrt{cs'^2 + bs' + a} + \frac{k^{-1}}{2\sqrt{c}} \log\left[2\sqrt{c(cs'^2 + bs' + a)} + 2cs' + b \right] \right\}_0^s \quad \text{(A5)}$$

Substituting for a, b, c and k^{-1} and evaluating Eq. (A5) yields

$$\int_0^s \mathrm{d}s' \sqrt{cs'^2 + bs' + a} = \frac{1}{2}\left\{ (s + r_0\cos\theta)\sqrt{s^2 + 2r_0 s\cos\theta + r_0^2} - r_0^2\cos\theta \right\}$$

$$+ \frac{1}{2}\left\{ r_0^2\sin^2\theta \log\left[2\left(\sqrt{s^2 + 2r_0 s\cos\theta + r_0^2} + s + r_0\cos\theta \right) \right] \right.$$

$$\left. - r_0^2\sin^2\theta \log\left[2(r_0 + r_0\cos\theta) \right] \right\} \quad \text{(A6)}$$

This can be further simplified by noting (again from the Law of Cosines) that $r_1 = \sqrt{s^2 + 2r_0 s\cos\theta + r_0^2}$. With that substitution and some rearrangement, Eq. (A6) becomes

$$\int_0^s \mathrm{d}s' \sqrt{cs'^2 + bs' + a} = \frac{1}{2}\left\{ sr_1 + r_0(r_1 - r_0)\cos\theta + r_0^2\sin^2\theta \log\left[\frac{r_1 + s + r_0\cos\theta}{r_0(1 + \cos\theta)} \right] \right\} \quad \text{(A7)}$$

ACPD
14, 19315–19356, 2014

So the final solution for τ becomes, combining Eqs. (A7) and (A3)

$$\tau = Bs + \frac{A}{2}\left\{ sr_1 + r_0(r_1 - r_0)\cos\theta + r_0^2 \sin^2\theta \log\left[\frac{r_1 + s + r_0\cos\theta}{r_0(1+\cos\theta)}\right]\right\} \quad \text{(A8)}$$

which can be evaluated using the definitions of A and B given in Eq. (A2). The expression Eq. (A8) has the proper limiting behavior: when $\theta = 0^\circ$, Eq. (A8) reduces to Eq. (2). This corresponds to the case of radiation propagating radially outward from the center of the Earth, so $r_1 = r_0 + s$ and Eq. (1) yields the result given in Eq. (2) when τ is a linear function of r. When $\theta = 180^\circ$, radiation propagates radially inward, $r_1 = r_0 - s$, and the argument of the logarithm in Eq. (A8) becomes indeterminate. Equation (A8) therefore cannot be used directly as an algorithm when $\theta = 180^\circ$, but it remains true that the value of τ should approach the expression given in Eq. (2) as the path becomes vertical, so the failure of Eq. (A8) for the $\theta = 180^\circ$ case can be easily avoided by reverting to Eq. (2) when $\theta \rightarrow 180^\circ$.

The far more consequential case is $\theta \rightarrow 90^\circ$ (nearly-tangent paths): the value of τ obtained from Eq. (2) always represents an underestimate, and can be over 2 % smaller than τ obtained from Eq. (A8), as shown in Fig. 17. As alluded to in Sect. 2, the L04 GSLS model made a partial correction for the error caused by using Eq. (2) to estimate τ in the tangent layer by estimating the variation of β within the tangent layer based on the profile of β in adjacent layers. But the L04 GSLS tangent layer approximation was imperfect, and no correction was made in the L04 GSLS model for τ in nearly-tangent layers, so Eq. (A8) represents a clear improvement in the current GSLS model.

Acknowledgements. The majority of the material presented in this paper first appeared as a poster in the 7th Atmospheric Limb Conference, which was hosted by the University of Bremen, Germany in June 2013. This research was supported by NASA GSFC through SSAI Subcontract 21205-12-043. The authors thank NASA and NOAA for supporting limb scattering research, and particularly recognize Didier Rault for years of leadership developing the OMPS LP algorithms. Larry Thomason and Terry Deshler shared helpful insights into the stratospheric aerosol problem. The SSAI and NOAA OMPS teams supported this research and contributed

ACPD
14, 19315–19356, 2014

many useful discussions, including Ghassan Taha, Larry Flynn, Zhong Chen, Philippe Xu, Tong Zhu, Nick Gorkavyi, Al Fleig, Jack Larsen, Mike Linda, Leslie Moy, and Peter Hall. Several Hampton University students contributed to studies that have improved the GSLS model, including Daryl Ludy, Simone Hyater-Adams, Ricardo Uribe, Curtis Driver, Jonathan Geasey, Nicholas Carletta, and Darel Davidson. We appreciate the OSIRIS, SCIAMACHY, SAGE II, SAGE III and U. of Wyoming measurement teams, for maintaining and sharing their high-quality data sets. Finally, we thank Alexei Rozanov and the U. of Bremen team for enabling remote participation in the 7th Atmospheric Limb Conference.

References

Bovensmann, H., Burrows, J. P., Buchwitz, M., Frerick, J., Noël, S., Rozanov, V. V., Chance, K. V., and Goede, A. P. H.: SCIAMACHY: mission objectives and measurement modes, J. Atmos. Sci., 56, 127–150, 1999. 19317

Bourassa, A. E., Degenstein, D. A., and Llewellyn, E. J.: SASKTRAN: a spherical geometry radiative transfer code for efficient estimation of limb scattered sunlight, J. Quant. Spectrosc. Rad., 109, 57–73, 2008. 19317

Chapman, S.: The absorption and dissociative or ionizing effect of monochromatic radiation in an atmosphere on a rotating Earth. Part II. Grazing incidence, Proc. Phys. Soc., 43, 483–501, 1931. 19326

Coulson, K. L., Dave, J. V., and Sekera, Z.: Tables related to radiation emerging from a planetary atmosphere, U. California, Berkeley, 1960. 19325

CRC: Standard Mathematical Tables, 27. edn., edited by: Beyer, W. H., CRC Press, Inc., Boca Raton, Florida, 1984. 19330

Deshler, T.: University of Wyoming stratospheric aerosol size distributions, http://www-das.uwyo.edu/~deshler/Data/Aer_Meas_Wy_read_me.htm, last access: February 2013. 19327, 19354

Deshler, T., Hervig, M. E., Hoffman, D. J., Rosen, J. M., and Liley, J. B.: Thirty years of in situ stratospheric aerosol size distribution measurements from Laramie, Wyoming (41° N), using balloon-borne instruments, J. Geophys. Res., 108, 4167, doi:10.1029/2002JD002514, 2003. 19327

ACPD
14, 19315–19356, 2014

Fitzmaurice, J. A.: Simplification of the Chapman function for atmospheric attenuation, Appl. Optics, 3, p. 640, 1964. 19326

Flittner, D. E., Bhartia, P. K., and Herman, B. M.: O_3 profiles retrieved from limb scatter measurements: theory, Geophys. Res. Lett., 27, 2601–2604, 2000. 19318

Flynn, L. E., Seftor, C. J., Larsen, J. C., and Xu, P.: The Ozone Mapping and Profiler Suite, Earth Science Satellite Remote Sensing, Volume 1: Science and Instruments, edited by: Qu, J., Gao, W., Kafatos, M., Murphy, R. E., and Salomonson, V. V., 279–295, Tsinghua University Press, Beijing and Springer, Berlin Heidelberg New York, doi:10.1007/978-3-540-37293-6, 2006. 19317

Griffioen, E. and Oikarinen, L.: LIMBTRAN: a pseudo three-dimensional radiative transfer model for the limb-viewing imager OSIRIS on the ODIN satellite, J. Geophys. Res., 105, 29717–29730, 2000. 19317

Herman, B. M., Ben-David, A., and Thome, K. J.: Numerical techniques for solving the radiative transfer equation for a spherical shell atmosphere, Appl. Optics, 33, 1760–1770, 1994. 19318, 19320

Herman, B. M., Caudill, T. R., Flittner, D. E., Thome, K. J., and Ben-David, A.: Comparison of the Gauss-Seidel spherical polarized radiative transfer code with other radiative transfer codes, Appl. Optics, 34, 4563–4572, 1995. 19318, 19320

Kyrölä, E., Tamminen, J., Leppelmeier, G. W., Sofieva, V., Hassinen, S., Bertaux, J. L., Hauchecorne, A., Dalaudier, F., Cot, C., Korablev, O., Fanton d'Andon, O., Barrot, G., Mangin, A., Théodore, B., Guirlet, M., Etanchaud, F., Snoeij, P., Koopman, R., Saavedra, L., Fraisse, R., Fussen, D., and Vanhellemont, F.: GOMS on ENVISAT: an overview, Adv. Space Res., 33, 1020–1028, doi:10.1016/S0273-1177(03)00590-8, 2004. 19317

Llewellyn, E. J., Lloyd, N. D., Degenstein, D. A., Gattinger, R. L., Petelina, S. V., Bourassa, A. E., Wiensz, J. T., Ivanov, E. V., McDade, I. C., Solheim, B. H., McConnell, J. C., Haley, C. S., von Savigny, C., Sioris, C. E., McLinden, C. A., Griffioen, E., Kaminski, J., Evans, W. F., Puckrin, E., Strong, K., Wehrle, V., Hum, R. H., Kendall, D. J. W., Matsushita, J., Murtagh, D. P., 5 Brohede, S., Stegman, J., Witt, G., Barnes, G., Payne, W. F., Piché, L., Smith, K., Warshaw, G., Deslauniers, D.-L., Marchand, P., Richardson, E. H., King, R. A., Wevers, I., McCreath, W., Kyrölä, E., Oikarinen, L., Leppelmeier, G. W., Auvinen, H., Mégie, G., Hauchecorne, A., Lefèvre, F., de La Nöe, J., Ricaud, P., Frisk, U., Sjoberg, F., von Schéele, F., and Nordh, L.: The OSIRIS instrument on the Odin spacecraft, Can. J. Phys., 82, 411–422, 2004. 19317

ACPD
14, 19315–19356, 2014

Loughman, R. P., Griffioen, E., Oikarinen, L., Postylyakov, O. V., Rozanov, A., Flittner, D. E., and Rault, D. F.: Comparison of radiative transfer models for limb-viewing scattered sunlight measurements, J. Geophys. Res., 109, D06303, doi:10.1029/2003JD003854, 2004. 19317, 19318, 19325, 19345

Loughman, R. P., Flittner, D. E., Herman, B. M., Bhartia, P. K., Hilsenrath, E., and McPeters, R. D.: Description and sensitivity analysis of a limb scattering ozone retrieval algorithm, J. Geophys. Res., 110, doi:10.1029/2004JD005429, 2005. 19324

McLinden, C. A. and Bourassa, A. E.: A systematic error in plane-parallel radiative transfer calculations, J. Atmos. Sci., 67, 1695–1699, 2010. 19317, 19324

McLinden, C. A., McConnell, J. C., Griffioen, E., and McElroy, C. T.: A vector radiative transfer model for the Odin/OSIRIS project, Can. J. Phys., 80, 375–393, 2002. 19317

McPeters, R. D., Janz, S. J., Hilsenrath, E., Brown, T. L., Flittner, D. E., and Heath, D. F.: The retrieval of O_3 profiles from limb scatter measurements: results from the shuttle ozone limb sounding experiment, Geophys. Res. Lett., 27, 2597–2600, 2000. 19317

Mishchenko, M. I., Lacis, A. A., and Travis, L. D.: Errors induced by the neglect of polarization in radiance calculations for Rayleigh-scattering atmospheres, J. Quant. Spectrosc. Ra., 51, 491–510, 1994. 19324, 19325

Natraj, V., Li, K., and Yung, Y. L.: Rayleigh scattering in planetary atmospheres: corrected tables through accurate computation of X and Y functions, Astrophys. J., 691, 1909–1920, 2009. 19325, 19338

Oikarinen, L., Sihvola, E., and Kyrölä, E.: Multiple scattering radiance in limb-viewing geometry, J. Geophys. Res., 104, 31261–31274, 1999. 19317

Postylyakov, O. V.: Radiative transfer model MCC++ with evaluation of weighting functions in spherical atmosphere for usage in retrieval algorithms, Adv. Space Res., 34, 721–726, 2004. 19317

Rault, D. F.: Ozone profile retrieval from SAGE III limb scattering measurements, J. Geophys. Res., 110, D09309, doi:10.1029/2004JD004970, 2005. 19317, 19318

Rault, D. and Loughman, R. P.: The OMPS limb profiler environmental data record algorithm theoretical basis document and expected performance, IEEE T. Geosci. Remote, 51, doi:10.1109/TGRS.2012.2213093, 2013. 19318, 19324, 19340

Rault, D. F. and Taha, G.: Validation of ozone profiles retrieved from Stratospheric Aerosol and Gas Experiment III limb scatter measurements, J. Geophys. Res., 112, D13309, doi:10.1029/2006JD007679, 2007. 19318

ACPD
14, 19315–19356, 2014

Rozanov, A., Rozanov, V., and Burrows, J. P.: A numerical radiative transfer model for a spherical planetary atmosphere: combined differential-integral approach involving the picard iterative approximation, J. Quant. Spectrosc. Ra., 69, 491–512, 2001. 19317

Spada, F., Krol, M. C., and Stammes, P.: McSCIA: application of the Equivalence Theorem in a Monte Carlo radiative transfer model for spherical shell atmospheres, Atmos. Chem. Phys., 6, 4823–4842, doi:10.5194/acp-6-4823-2006, 2006. 19317

Taha, G., Jaross, G., Fussen, D., Vanhellemont, F., Kyrölä, E., and McPeters, R. D.: Ozone profile retrieval from GOMOS limb scattering measurements, J. Geophys. Res., 113, D23307, doi:10.1029/2007JD009409, 2008. 19318

Whitney, C. K.: The DART Method, Standard Procedures to Compute Radiative Transfer in a Scattering Atmosphere, edited by: Lenoble, J., Radiation Commission, International Association of Meteorology and Atmospheric Physics, I.U.G.G., published by National Center for Atmospheric Research, Boulder, Colorado, 80–83, 1977. 19317

ACPD
14, 19315–19356, 2014

Table 1. Cases for which the L04 and current GSLS radiances are compared to Siro radiances.

λ (nm)	325, 345, 600 nm
h (km)	10–60 km (5 km steps)
θ_T (°)	15, 60, 80, 90
ϕ_T (°)	20, 90, 160

ACPD
14, 19315–19356, 2014

Table 2. Cases studied to determine the appropriate number of MS zeniths to be used in the GSLS model.

λ (nm)	325, 345, 600 nm
h (km)	10–60 km (5 km steps)
θ_T (°)	15, 45, 60, 70, 80, 85
ϕ_T (°)	0, 20, 40, 60, 80, 90, 100, 120, 140, 160, 180

ACPD
14, 19315–19356, 2014

Table 3. Cases used to verify the GSLS polarized radiance by comparison to the results of Natraj et al. (2009). The cases are identified by the cosine of the solar zenith angle μ_0, the Lambertian surface reflectivity R, and the Rayleigh scattering optical depth τ_R.

μ_0	0.2, 1.0
R	0, 0.8
τ_R	0.5, 1.0

ACPD
14, 19315–19356, 2014

Table 4. Aerosol size distribution details for the simulated radiances shown in Fig. 15. Each size distribution is bi-modal log-normal, and is therefore defined by the concentration N, mode radius r, and standard deviation σ for fine and coarse particle modes (indicated by subscript f and c, respectively).

	ASD20	ASD25
N_f (cm^{-3})	6.57167	5.71833
r_f (nm)	76.55	51.05
σ_f	1.310	1.43833
N_c (cm^{-3})	0.53642	0.23473
r_c (nm)	264.533	202.5
σ_c	1.485	1.150

ACPD
14, 19315–19356, 2014

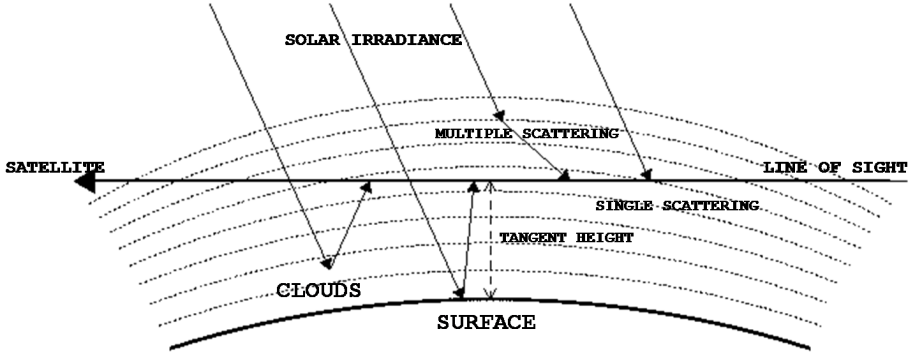

Figure 1. Illustration of the limb scattering viewing geometry (from Rault and Loughman, 2013).

ACPD
14, 19315–19356, 2014

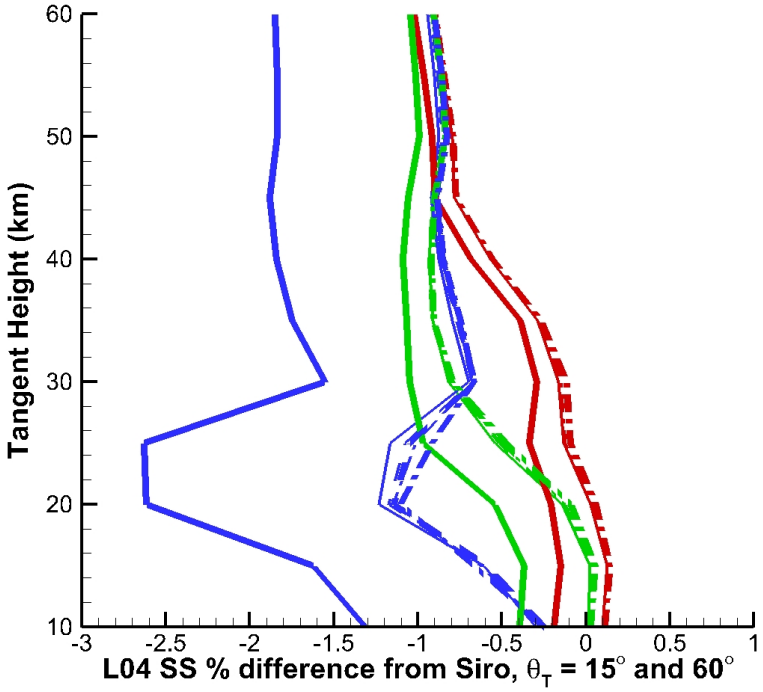

Figure 2. Comparison of L04 GSLS SS radiances to Siro SS radiances for the λ and ϕ_T cases listed in Table 1, at $\theta_T = 15^\circ$ (thin lines) and 60° (thick lines). Color-coding indicates λ (red = 325 nm, green = 345 nm, blue = 600 nm), while line type indicates ϕ_T (solid = 20°, dashed = 90°, dot-dashed = 160°).

ACPD
14, 19315–19356, 2014

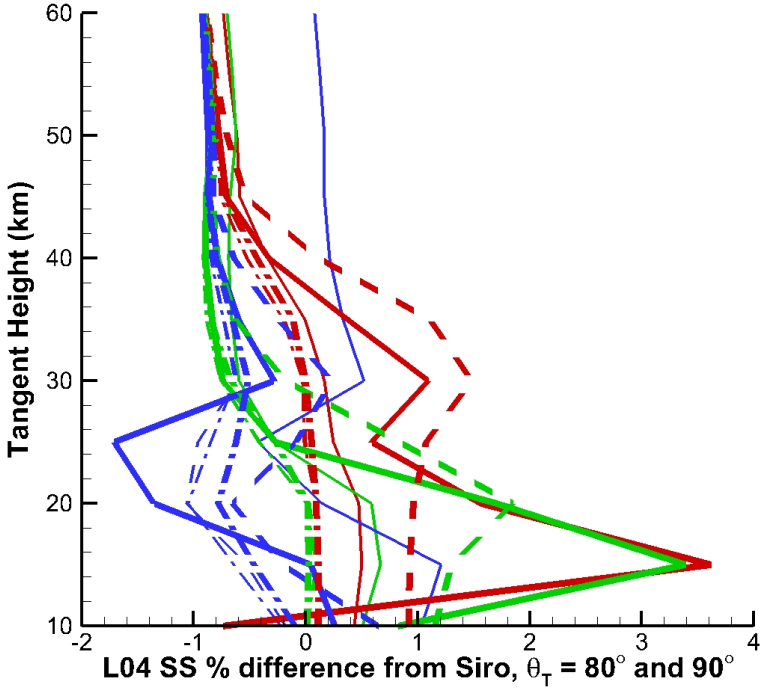

Figure 3. Comparison of L04 GSLS SS radiances to Siro SS radiances for the λ and ϕ_T cases listed in Table 1, at $\theta_T = 80^\circ$ (thin lines) and 90° (thick lines). Color-coding and line type have the same meaning as in Fig. 2.

ACPD
14, 19315–19356, 2014

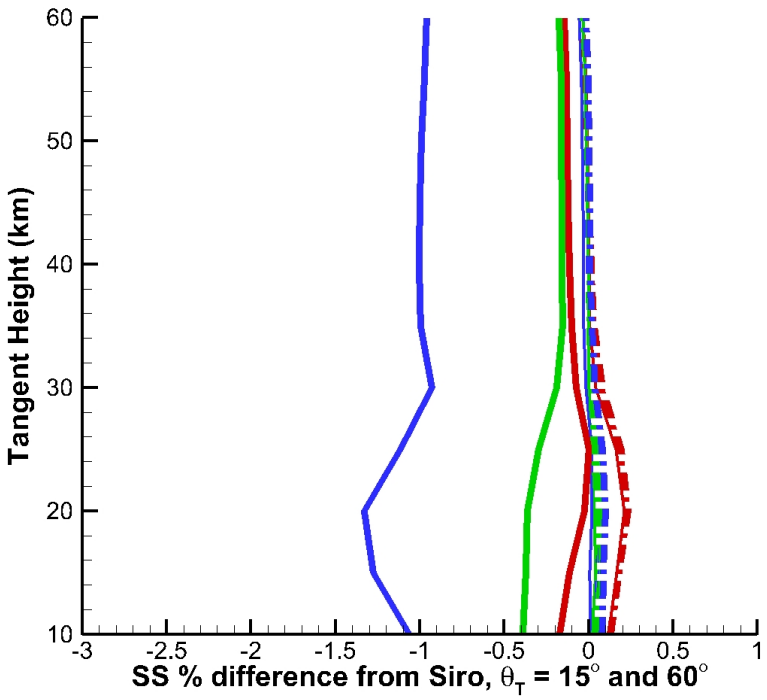

Figure 4. Comparison of current GSLS SS radiances to Siro SS radiances for the λ and ϕ_T cases listed in Table 1, at $\theta_T = 15^\circ$ (thin lines) and 60° (thick lines). Color-coding and line type have the same meaning as in Fig. 2. The improved agreement relative to Fig. 2 results arises from allowing β to vary linearly with altitude in the current GSLS model.

ACPD
14, 19315–19356, 2014

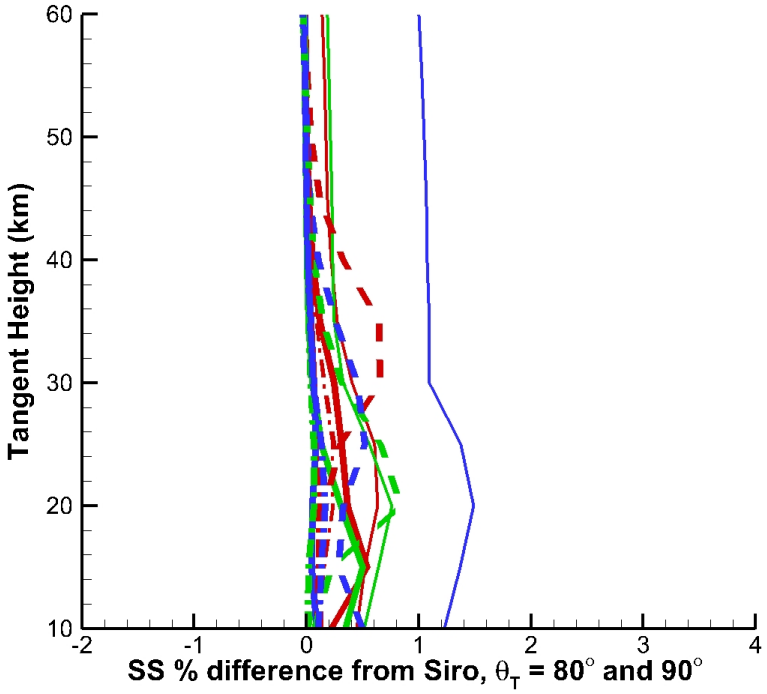

Figure 5. Comparison of current GSLS SS radiances to Siro SS radiances for the λ and ϕ_T cases listed in Table 1, at $\theta_T = 80^\circ$ (thin lines) and 90° (thick lines). Color-coding and line type have the same meaning as in Fig. 2. The improved agreement relative to Fig. 3 results arises from allowing β to vary linearly with altitude in the current GSLS model.

ACPD
14, 19315–19356, 2014

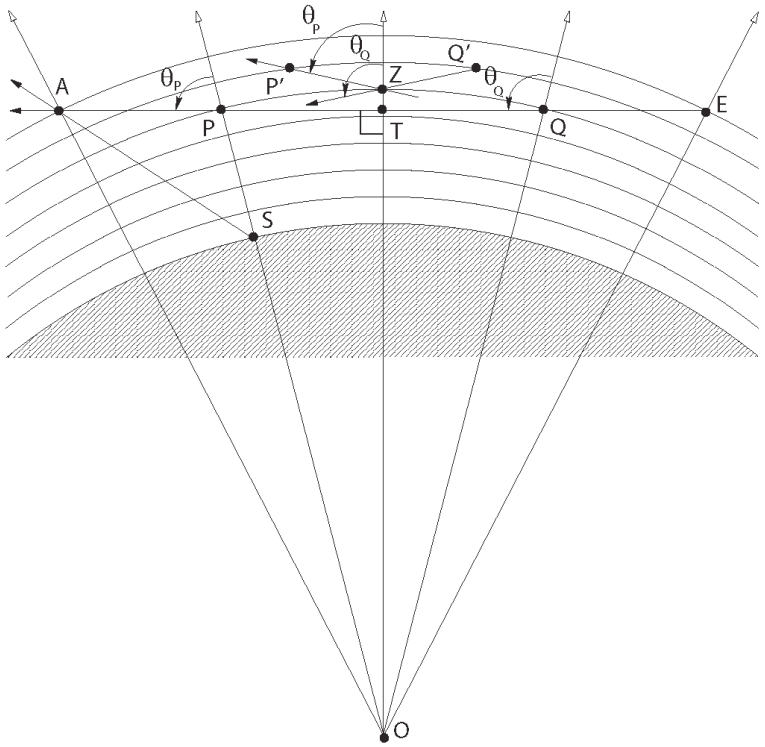

Figure 6. Illustration of the LS geometry. The radiation travels along the LS LOS from the TOA at point *E* downward to the tangent point *T*, then upward to the TOA at *A*. Zeniths originate at the center of the spherical Earth *O* and radiate outward through the atmosphere (from Fig. 9 of Loughman et al., 2004).

ACPD
14, 19315–19356, 2014

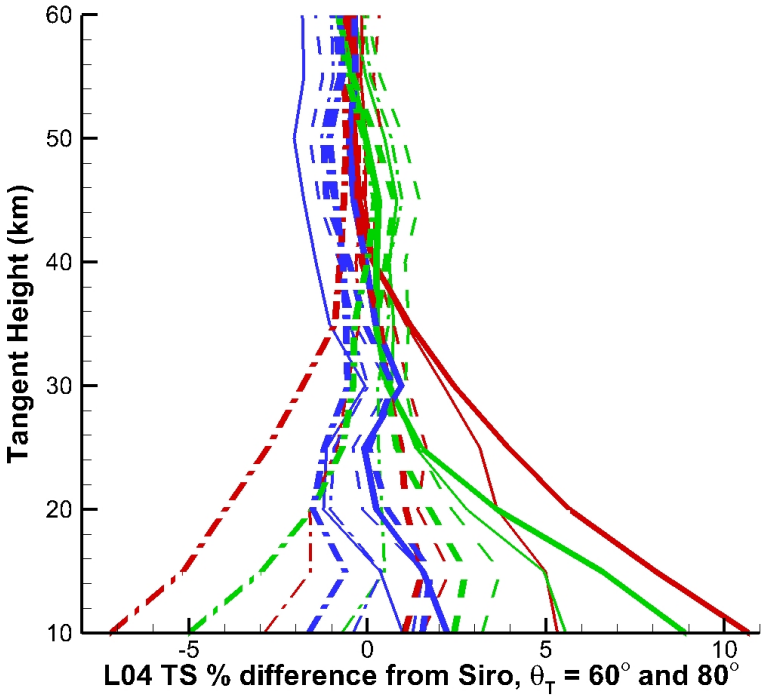

Figure 7. Comparison of L04 GSLS TS radiances to Siro TS radiances when $R = 0.95$ for the λ and ϕ_T cases listed in Table 1, at $\theta_T = 60^\circ$ (thin lines) and 80° (thick lines). Color-coding and line type have the same meaning as in Fig. 2.

ACPD
14, 19315–19356, 2014

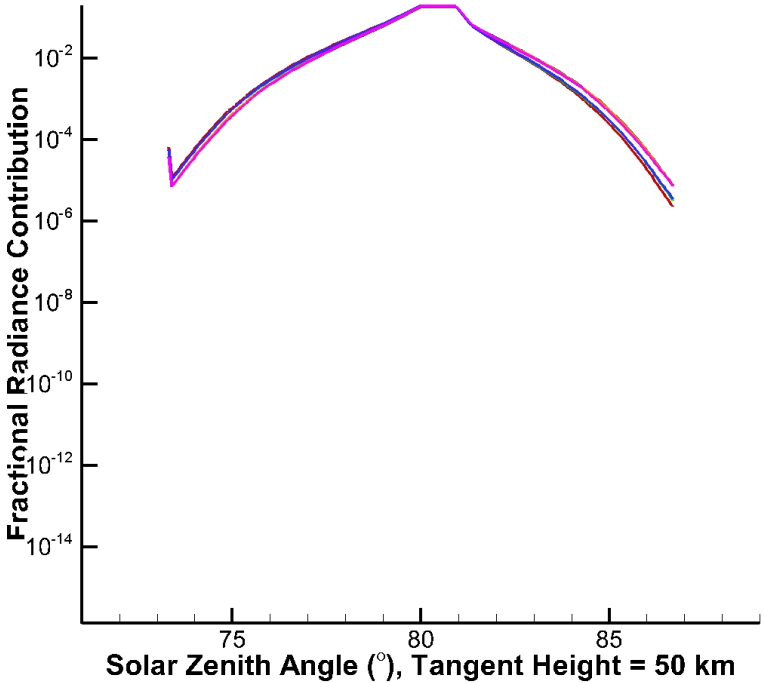

Figure 8. Relative contribution for the layers along the LOS for $\theta_T = 80^\circ$, $\phi_T = 20^\circ$, $R = 0.95$, and $h = 50$ km. The MS radiance relative contributions are shown for $\lambda = 325, 345$ and 600 nm as red, green, and blue lines, respectively, while the SS radiance contributions are shown as gray, orange, and pink lines, respectively.

ACPD
14, 19315–19356, 2014

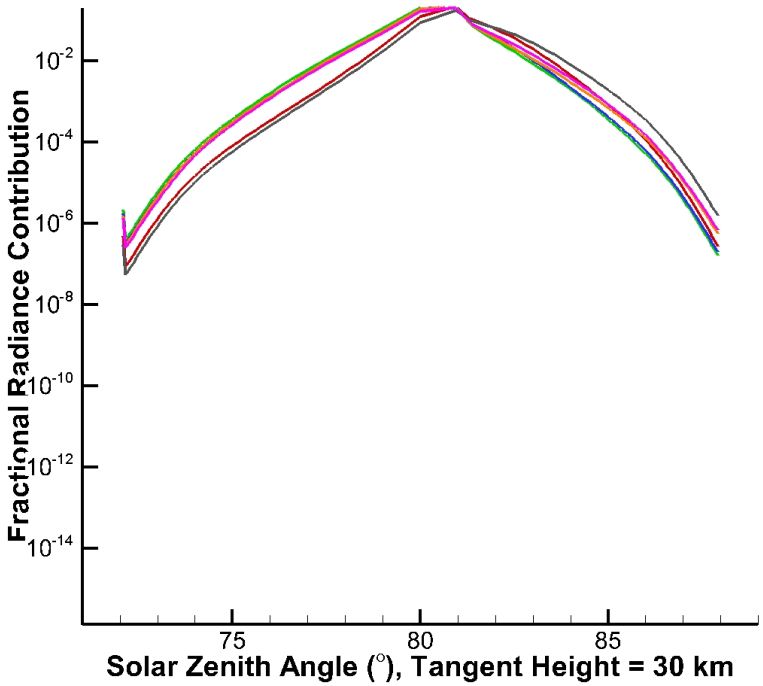

Figure 9. Same as Fig. 8, except h = 30 km.

ACPD
14, 19315–19356, 2014

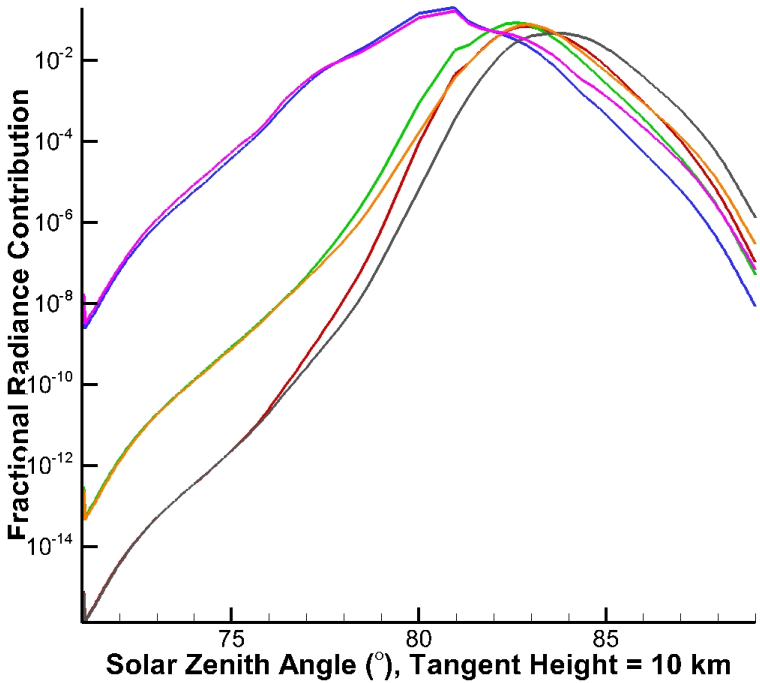

Figure 10. Same as Fig. 8, except h = 10 km.

ACPD
14, 19315–19356, 2014

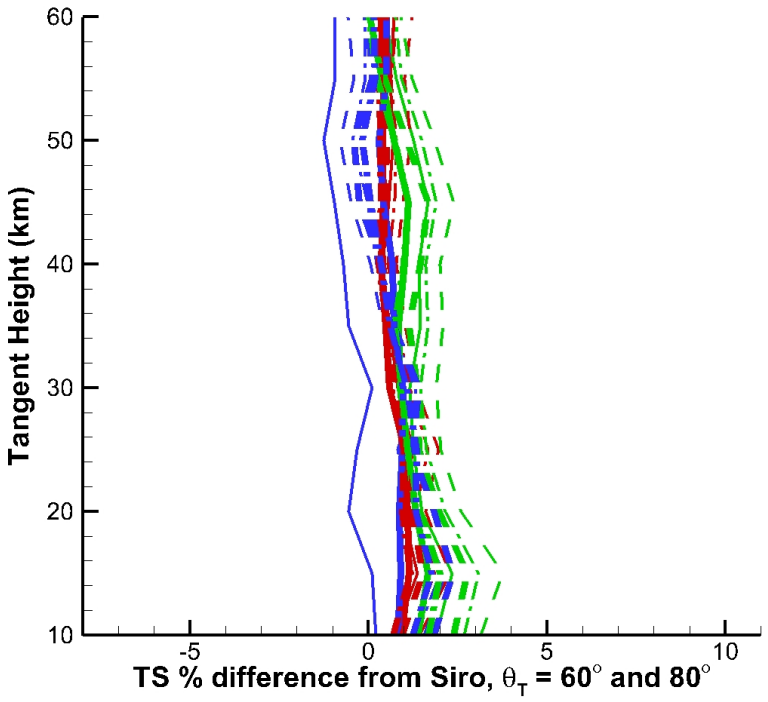

Figure 11. Comparison of current GSLS TS radiances to Siro TS radiances when R = 0.95 for the λ and ϕ_T cases listed in Table 1, at $\theta_T = 60^\circ$ (thin lines) and 80° (thick lines). Color-coding and line type have the same meaning as in Fig. 2. The improved agreement relative to Fig. 7 results arises from the introduction of multiple MS zeniths in the current GSLS model.

ACPD
14, 19315–19356, 2014

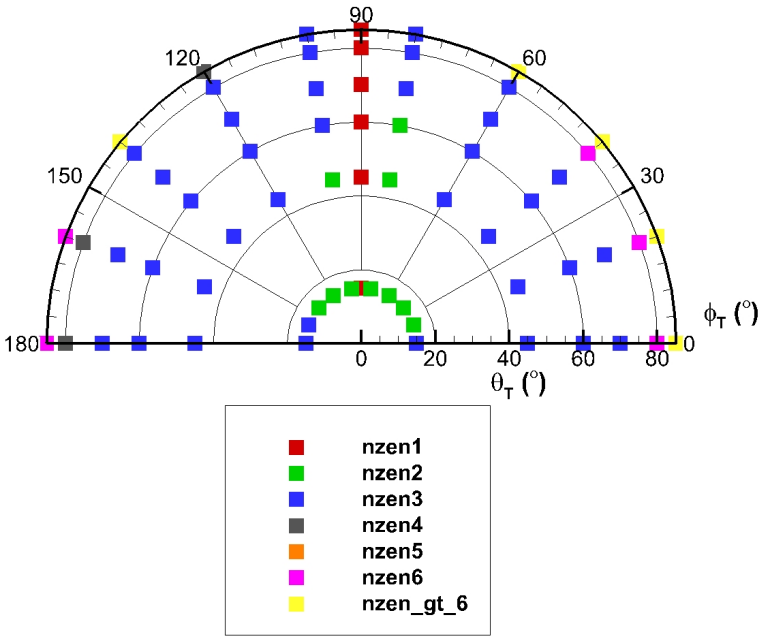

Figure 12. The number of MS zeniths needed to cause the calculated GSLS TS radiance to agree with the reference calculations (which use 143 MS zeniths) to within 0.2% at all λ and h. This analysis is illustrated for each of the θ_T and ϕ_T values listed in Table 2.

ACPD
14, 19315–19356, 2014

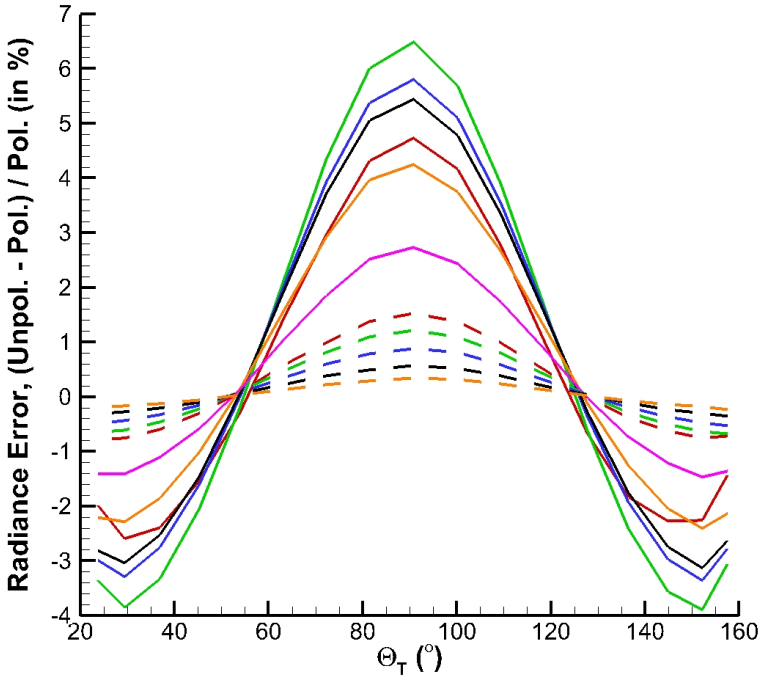

Figure 13. The TS radiance error that results from neglecting polarization is plotted as a function of SS angle Θ_T for a series of radiance simulations that employ the viewing geometry of a simulated NPP OMPS LP orbit. The tangent height h = 40 km, R = 0, and the curves indicate the error associated with λ = 325, 345, 385, 400, 449, 521 nm (red, green, blue, gray, orange and pink solid lines) and λ = 602, 676, 756, 869, 1020 nm (red, green, blue, gray, orange dashed lines).

ACPD
14, 19315–19356, 2014

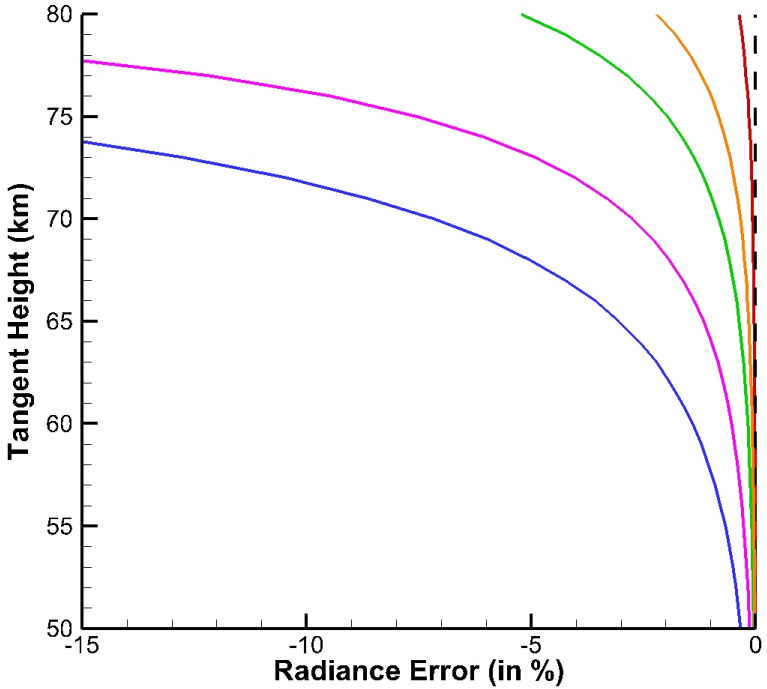

Figure 14. Total radiance error caused by changes in the TOA altitude and treatment of the atmosphere above the TOA. The reference radiance profile is calculated with TOA = 100 km and the Chapman layer included above the TOA. Retaining the Chapman layer but reducing the TOA altitude produces the radiance error illustrated by orange (TOA = 90 km) and pink (TOA = 80 km) lines, respectively. Removing the Chapman layer causes additional error, illustrated as red (TOA = 100 km), green (TOA = 90 km) and blue (TOA = 80 km) lines, respectively.

ACPD
14, 19315–19356, 2014

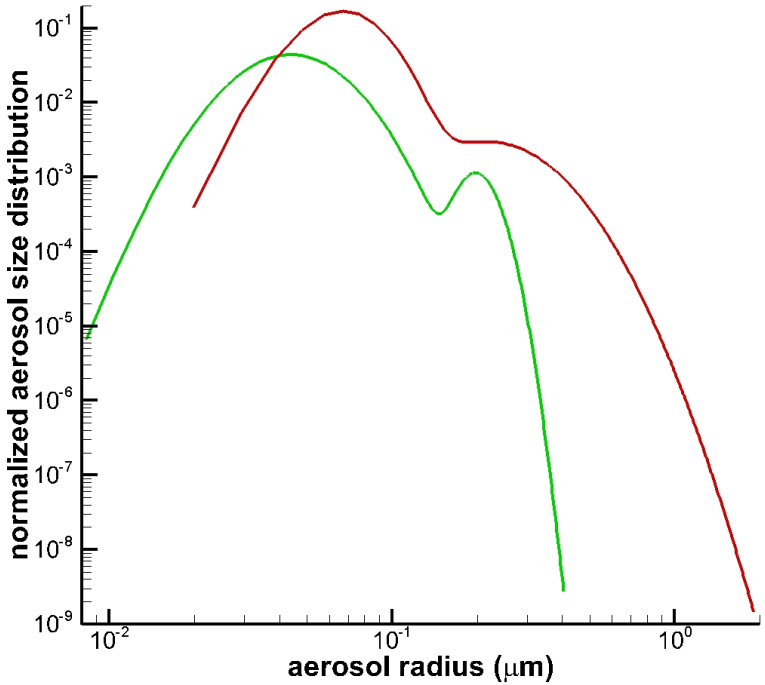

Figure 15. Illustration of the normalized aerosol size distributions for two bi-modal log-normal stratospheric aerosol cases. The two distributions were calculated by averaging the individual ASD properties retrieved during 6 balloon flights over Laramie, Wyoming during 2012 (Deshler, 2013). The red line indicates the ASD20 size distribution (derived from observations at altitude $z = 20$ km), while the green line indicates the ASD25 size distribution (derived from observations at $z = 25$ km). The details of these two ASDs are given in Table 4.

ACPD
14, 19315–19356, 2014

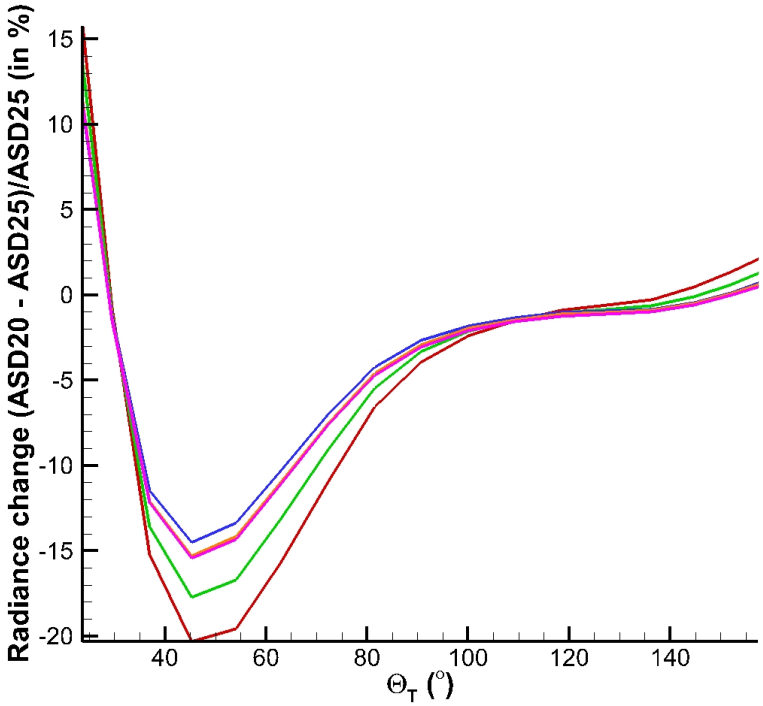

Figure 16. Comparison of TS radiances at $\lambda = 600$ nm for $h = 20, 25, 30, 35$, and 40 km (shown by red, green, blue, orange, and pink lines, respectively). The two aerosol size distributions plotted in Fig. 15 are used in the two sets of radiances compared, with all other quantities (including aerosol extinction coefficients) held constant.

ACPD
14, 19315–19356, 2014

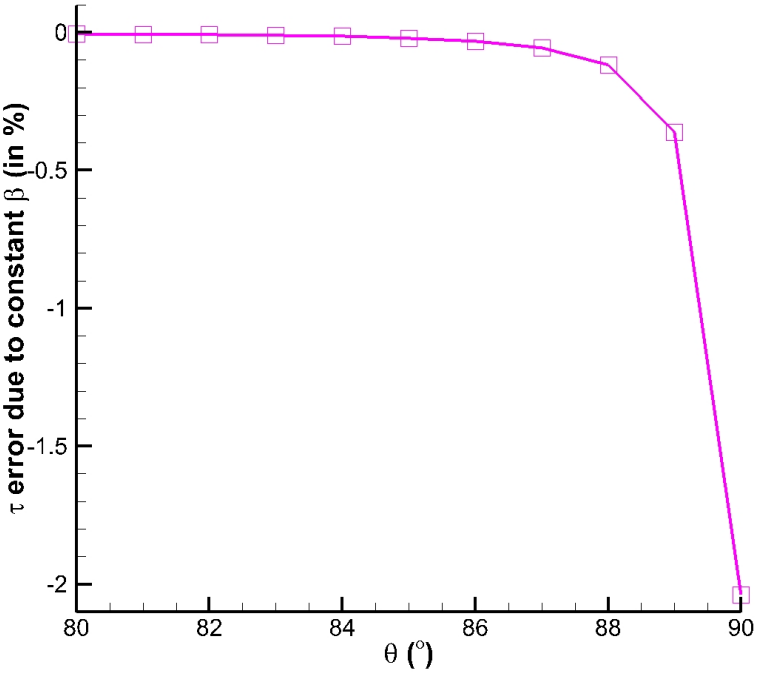

Figure 17. Percentage difference between the value of τ obtained from Eq. (2) and the value of τ obtained from Eq. (A8), as a function of θ. The LOS has h = 60 km in this example.

ACPD
14, 19315–19356, 2014